

Development and Multifunctional Characterization of a Structural Sodium-Ion Battery Using a High-Tensile-Strength Poly(ethylene oxide)-Based Matrix Composite

Vasan Iyer,* Jan Petersen, Sebastian Geier, and Peter Wierach

Cite This: *ACS Appl. Energy Mater.* 2024, 7, 3968–3982

Read Online

ACCESS |

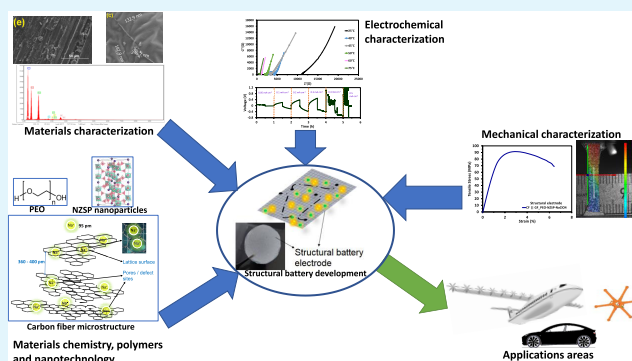
Metrics & More

Article Recommendations

Supporting Information

ABSTRACT: Structural batteries are gaining attention and can play a significant role in designing emission-free lightweight defense and transport systems such as aircraft, unmanned air vehicles, electric cars, public transport, and vertical takeoff and landing (VTOL)-urban air traffic. Such an approach of integrated functions contributes to overall mass reduction, high performance, and enhanced vehicle spaciousness. The present work focuses on developing and characterizing multifunctional structural sodium-ion battery components by using a high-tensile-strength structural electrolyte (SE) prepared by incorporating a glass fiber sandwiched between thin solid-state poly(ethylene oxide)-based composite electrolyte layers. The electrochemical and mechanical characterization of the structural electrolyte shows multifunctional performance with a tensile strength of 40.9 MPa and an ionic conductivity of $1.02 \times 10^{-4} \text{ S cm}^{-1}$ at 60 °C. It displays an electrochemical window of 0 to 4.5 V. The structural electrode is fabricated using a heat press by pressing intermediate-modulus carbon fibers (CFs) against the structural electrolyte, and it shows a high tensile strength of 91.3 MPa. The fabricated structural battery CF||SE||Na provides a typical energy density of 23 Wh kg⁻¹ and performs 500 cycles while retaining 80% capacity until 225 cycles. The investigation of sodium structural battery architecture in this preliminary work demonstrates intercalation of sodium ions in intermediate modulus-type carbon fiber electrodes, shows multifunctional performance with excellent cycling stability and structural strength, and provides an alternative path to current structural battery designs.

KEYWORDS: structural sodium batteries, structural energy storage, multifunctional materials, carbon fiber electrode, multifunctional power composites



1. INTRODUCTION

The transportation industry needs rapid development in energy storage technologies in order to achieve sustainable growth and to cut down emissions to tackle global warming. The European Green Deal sets an arduous target of achieving this goal by 2050.¹ Additionally, roadmaps specifically have been put forward for the aviation industry by Europe and the US to reduce environmental pollution.^{2–4} To address these ambitious tasks, an excellence cluster called Sustainable and Energy Efficient Aviation (SE2A), funded by the German research foundation (Deutsche Forschungsgemeinschaft (DFG)) promoting interdisciplinary research, was initiated in the year 2019 to investigate new technologies for sustainable aviation.⁵ One of the strategies researched within the cluster to cut down aircraft emissions is through more electrification of aircraft systems by means of structural energy storage systems. These systems are multifunctional and have the capability to store energy as well as provide structural support (ability to endure loads) simultaneously.^{6,7} This will help to build lightweight systems and improve overall efficiency and space

utilization.^{8–10} Conventionally, electrical energy is stored in the form of batteries, supercapacitors, fuel cells, etc. Some of the problems with conventional batteries are overall increased system mass, space allocation, and usage of liquid electrolytes, which have no ability to withstand loads and also pose considerable safety issues.⁸ By integration of energy storage into load-carrying structures, also known as structure integration, these issues can be addressed. Figure 1 shows the various concepts of multifunctional structural energy storage, possible routes to achieve multifunctionality or structure integration, and the degrees of integration (DOI). In conventional energy storage systems DOI 0, the energy

Received: February 2, 2024

Revised: April 5, 2024

Accepted: April 5, 2024

Published: April 14, 2024



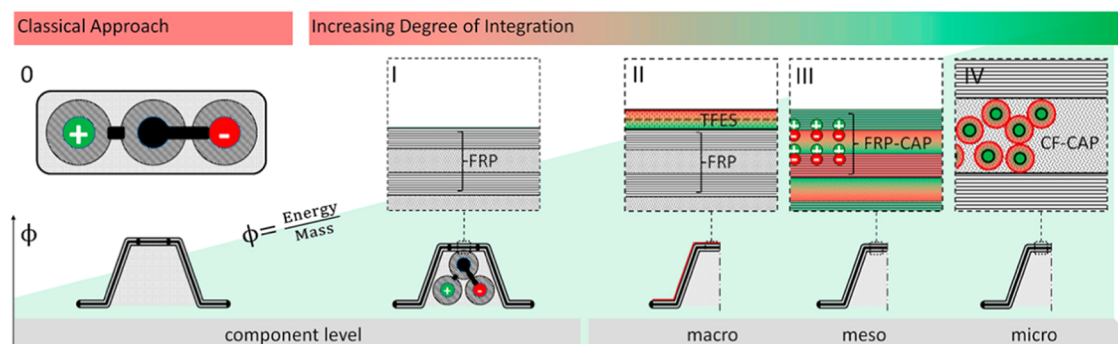


Figure 1. Concept and scales of multifunctional structural energy storage demonstrated for an aircraft fuselage omega stringer are shown below, and a laminate structure is shown above: classical functional separation (0), integration of nonload-carrying conventional cells (I), integrated thin-film energy storages (II), structural laminate storages (III), and microscaled constituent functionalization (IV). Reproduced with permission.⁸ Copyright 2018, MDPI.

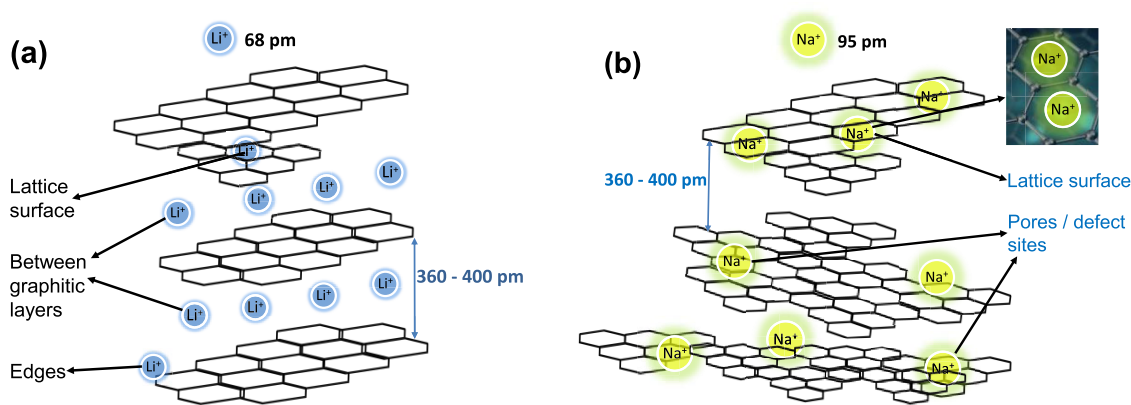


Figure 2. Illustration showing the typical intercalation mechanism in an intermediate-modulus carbon fiber: (a) Li-ion size and intercalation inside the carbon fiber graphitic microstructure. (b) Na-ion size and intercalation inside the carbon fiber graphitic microstructure.

storage device and the structure are separated, and these energy storage devices provide no structural support. In DOI I, the energy storage devices are embedded in the unused spaces within the structure.^{11,12} DOI II is achieved by the use of energy storage in thin films that are attached to the surface or placed into a composite laminate, which adds a certain amount of structural capabilities by providing more tensile strength.^{13–15}

From DOI III, the multifunctionality of individual components increases, where all constituents have specific roles, tasks, and multiple abilities such as ion storage and ability to withstand loads.^{16,17} For higher degrees of integration, the use of functionalized carbon fibers (CF), which possess both mechanical and electrochemical properties, is an important component for developing multifunctional energy storage materials.^{18–21} Studies using CF as electrodes in structural supercapacitors were reported in the past.^{22–24} In DOI IV, also called coaxial integration, each coaxial fiber constituent is functionalized to work as an independent energy storage device.²⁵ The 3D-type structural battery with carbon fiber electrodes coated with a polymer electrolyte and a counter electrode of lithium metal is an example of DOI IV integration.²⁶

Structural batteries, when compared to conventional batteries using liquid electrolytes, pose considerable challenges when it comes to balancing mechanical and electrochemical performance.^{7,9,27} The key technological steps to realize efficient structural batteries with higher DOI include develop-

ment of a structural cathode and optimization of the structural and electrochemical properties of the electrolyte material.^{28–31} In the past several approaches to structural battery designs were investigated; the first approach is by embedding thin-film batteries inside a composite laminate, the second approach is by using the polymer matrix both as an electrolyte and as a structural binder for the fibers, and the third approach is by using an all-solid-state polymer electrolyte.^{31–34}

The pathway to create structural batteries with a higher degree of integration (DOI III–IV) is by insertion of ions into carbon fibers (CFs), which are used as electrodes. Studies were made in the past regarding lithium-ion insertion into carbon fiber microstructures using different types of carbon fibers in structural batteries.^{19,21,35,36} The use of carbon fibers in structural batteries further enhances its properties, as they contribute to mechanical strength and can also act as electrodes.^{28–30} It was reported that the intermediate-modulus (IM) carbon fibers showed a high electrochemical capacity of 177 mAh g⁻¹ (with sizing), whereas high-modulus (HM) carbon fibers showed only 154 mAh g⁻¹.^{18,29,31} This is due to the type of carbon fiber microstructure associated with these types of fibers. While the HM carbon fibers have an ordered graphitic microstructure, in which the lithium-ion intercalates between the graphitic layers, the IM carbon fibers have disordered carbon microstructures offering additional lattice surfaces and edges, which further allows Li-ion insertion (as shown in Figure 2a).^{37,38} These studies suggested lithium-ion-based structural batteries using a bicontinuous-phase-type

electrolyte as a successful approach to achieve integration with carbon fibers.^{29,32} Recently, lithium-ion structural batteries based on an all-solid-state composite-type electrolyte were also reported to have shown a capacity of 1.45 mAh cm⁻² and a tensile strength of 124.2 MPa.³³ In contrast, studies regarding sodium-ion conducting polymer electrolytes and, in particular, sodium-ion insertion into carbon fibers are few and need further investigation, especially for structural energy storage applications.^{39–45} The present work is an attempt to address this gap. While a lithium ion intercalates in lattice surfaces, in-between graphitic layers, and edges (Figure 2a), the sodium ion intercalates mostly in the lattice surface, nanopores, or defect sites found in disordered carbons and is prevalent in the IM-type carbon fibers (shown in Figure 2b).^{21,41} Hence, the IM-type CF is chosen as a suitable fiber type for present work.

The selection of a polymer matrix plays a key role in achieving multifunctionality in a structural battery. PEO (poly(ethylene oxide))-based electrolytes with alkali metal salts dissolved in them are reported to display low ionic conductivities at room temperatures, not suitable for battery operation.^{46,47} They are also known to feature dendrite issues, which hinder the development of successful batteries as it leads to the gradual destruction of the separator.^{48,49} However, addition of inorganic ceramic fillers to PEO in the development of a composite solid electrolyte (CSE) has been shown to make the PEO polymer amorphous (less crystalline), improve its mechanical properties, and is shown to suppress the growth of sodium dendrites.^{50–52} Past studies have also shown that in amorphous regions, molecular chains are able to oscillate above their glass transition temperature and provide pathways for ion mobilization, and hence high ion conductivity.^{53,54} Additionally, the adhesive nature of PEO helps in the fabrication of the structural electrolyte by embedding glass fibers, which further improves its mechanical properties. It also acts as a structural binder for lamination with carbon fibers and provides a good interface. This led to the motivation to use PEO with inorganic ceramic nanoparticle fillers as the matrix for the present work.

In this study, sodium structural battery components are fabricated and investigated for their multifunctional performance to compare with the existing structural battery design approaches with higher DOI. To the best of the authors' knowledge, according to the available literature, this is the first study that investigates the sodium-ion insertion into carbon fibers using an all-solid-state composite-type electrolyte. The battery is fabricated in a novel way using chemistries that enable good sodium-ion conductivity. A two-step approach (solution casting followed by heat pressing) is used in fabricating the multifunctional structural components. The poly(ethylene oxide)-based matrix was added with sodium-rich inorganic ceramic NASICON-type Na₃Zr₂Si₂PO₁₂ (NZSP) active nanoparticle fillers to boost Na⁺-ion conductivity, and the composite solid electrolyte was prepared using a solution casting technique. It was then reinforced with glass fibers (GFs) using a heat press to obtain the structural electrolyte (GF_PEO-NZSP-NaClO₄) having a tensile strength of 40.9 MPa. The structural electrode was fabricated with IM-type carbon fibers by heat pressing with a structural electrolyte, and it displayed a very high tensile strength of 91.3 MPa. The structural battery CF||GF_PEO-NZSP-NaClO₄||Na provided a typical discharge capacity of 23 Wh kg⁻¹ for a 0.1C rate and performed 500 cycles with a capacity retention of 80% up to 225 cycles.

2. EXPERIMENTAL SECTION

2.1. Chemicals and Materials. Chemicals and materials for the synthesis of a structural electrolyte include poly(ethylene oxide) (PEO with a molecular weight $M_w = 10^6$ g mol⁻¹, Sigma-Aldrich), anhydrous acetonitrile (ACN, Sigma-Aldrich), sodium perchlorate (NaClO₄, Sigma-Aldrich), and sodium zirconium silico phosphate (Na₃Zr₂Si₂PO₁₂) or NZSP powder purchased from 421 Energy LLC, South Korea. A glass fiber woven fabric with an aerial weight of 163 g m⁻² and spread tow carbon fibers (CFs) Tenax IMS 65 24k tows with an aerial weight of 55 g m⁻² for the preparation of a structural electrolyte and a structural battery half-cell were purchased from R&G Faserverbundwerkstoffe GmbH, Germany. Pure sodium metal sticks for a structural battery counter electrode were purchased from Alfa Aesar. Two-sided siliconized papers for heat press were given free of cost from Laufenberg GmbH, Krefeld, Germany.

2.2. Preparation of NZSP Nanoparticles. The as-received NZSP (Na₃Zr₂Si₂PO₁₂) powder was wet ball-milled using a Fritsch planetary ball mill Pulverisette 7 (manufactured by FRITSCH GmbH, Germany). Overall, 3 g of the NZSP powder was mixed with 15 mL of isopropanol to the required consistency in each bowl consisting of 100 g of zirconium oxide (ZrO₂) balls of a 0.5 mm diameter, and the mixture was ball-milled for 12 h intermittently at a speed of 800 rpm with required time for cooling to prevent overheating inside the bowls. The obtained mixture containing nanoparticles was sonicated for 2 h to prevent agglomeration and then dried completely by heating (to evaporate all of the isopropanol in the mixture) to get pure NZSP nanoparticles.

2.3. Material Characterization and Analysis. The particle size characterization of the collected nanoparticles after ball-milling was done using a centrifuge particle sizing (CPS) instrument (as shown in Figure S1). In the CPS analyzer, a disc was inserted, and the initial starting speed was set to 8100 rpm. Once the analyzer was activated, a ramp speed of 21,000 rpm was set. Now, the 5 and 15% methyl ethyl ketone (MEK) solution was injected into the centrifuge in 10 different steps in various proportions to build a gradient inside the centrifuge. The centrifuge was made to run for 25 to 30 min; now, the diamond particle in the MEK solution was injected into the analyzer for calibration purposes, followed by NZSP nanoparticles in the MEK solution (2% mass fraction). The CPS instrument gave the particle size distribution (PSD) data, which were further confirmed using scanning electron microscopy (SEM) measurements. The SEM (FEI, Thermo Fisher Scientific Inc.) and X-ray diffraction techniques were used to study the morphology and characterize the structure of NZSP particles and also the prepared structural electrolyte and the electrode.

2.4. Preparation of Thin Polymer Membranes. Thin polymer membranes were prepared as described in the process chain, as shown in Figure S3. Initially, the Na₃Zr₂Si₂PO₁₂ (NZSP) powder immersed in an isopropanol solution was wet ball-milled for 12 h for production of nanoparticles. Meanwhile, 0.89 g of PEO and 0.165 g of NaClO₄ were added to 15 mL of an acetonitrile (ACN) organic solvent, and the ratio of ethylene oxide (–CH₂–CH₂–O–) to a sodium ion (EO:Na⁺) was maintained at 15:1; the sealed container containing the mixture was stirred for 4 h. Simultaneously, the obtained nanoparticles in the solution form after ball-milling were sonicated (using Branson 250 Digital Sonifier) with 20% pulsed amplitude for 4 h to prevent agglomeration. The obtained nanoparticles in isopropanol after sonication were heated until all of the isopropanol was evaporated, resulting in pure NZSP nanoparticles. Then, various amounts (0, 15, 25, and 30 wt %) of the collected nanoparticles were added to the already stirred solution mixture. The mixture was sonicated for a few hours and again stirred for further 20 h until a homogeneous mixture was obtained. The homogeneous mixture was then cast into a PTFE dish using a doctor's blade to get a smooth layer and left undisturbed in the fumehood for 6 h until a uniform layer was formed. The obtained membranes were vacuum-dried at 55 °C to get thin polymer membranes. The thickness of the membrane was measured to be 180 μm.

2.5. Preparation of the Structural Electrolyte. Structural electrolytes with a uniform thickness of 420 μm were prepared by

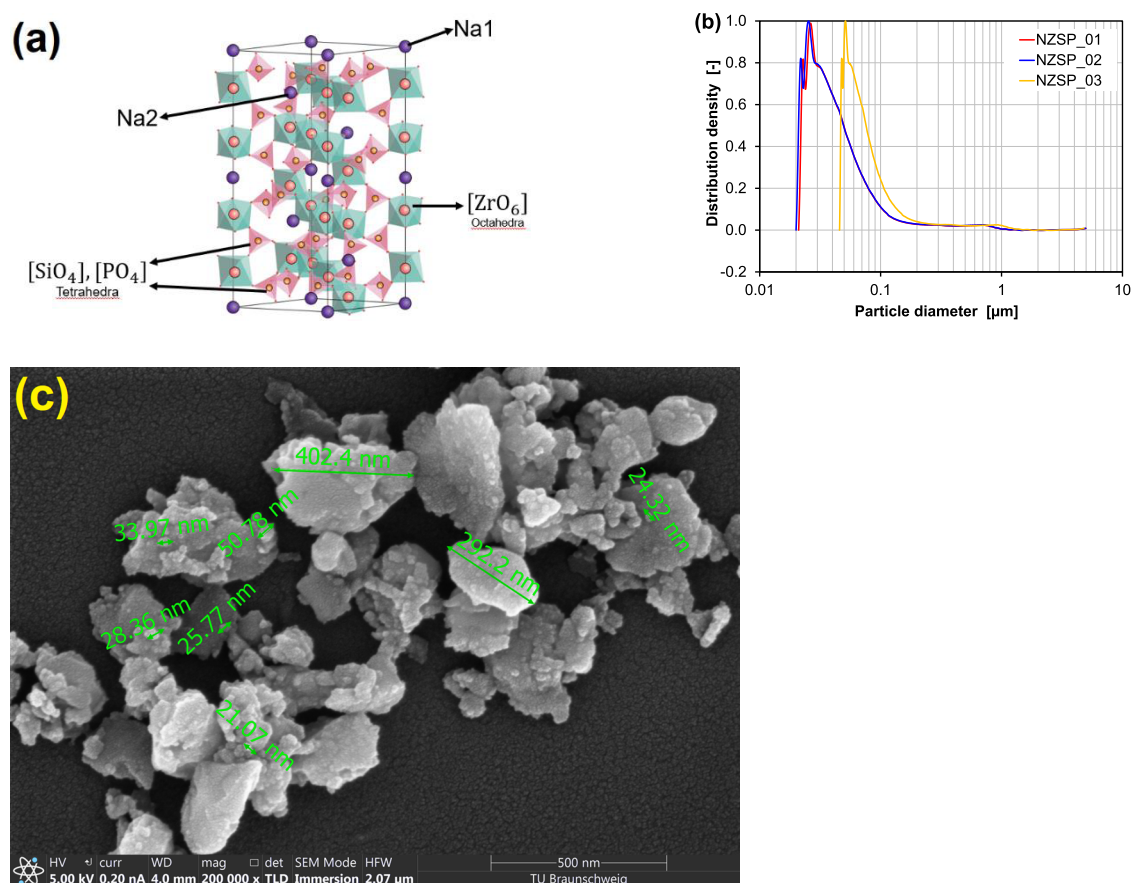


Figure 3. (a) Chemical structure of NZSP. Reproduced with permission.⁵⁷ Copyright 2018, Wiley. (b) NZSP nanoparticle size distribution plot obtained from the CPS analyzer. (c) Scanning electron microscopy image of NZSP nanoparticles.

placing the glass fiber sandwiched between two thin polymer membranes, and then it was heat-pressed (using Collins P500S press, COLLIN Lab & Pilot Solutions GmbH Maitenbeth, Germany) at 90 °C, 10 MPa for 25 min.

2.6. Preparation of the Structural Electrode. Structural electrodes were prepared by hot pressing (using Collins P500S press, COLLIN Lab & Pilot Solutions GmbH Maitenbeth, Germany) a single layer of a spread tow carbon fiber and the already prepared structural electrolyte at 100 °C, 10 MPa for 35 min.

2.7. Preparation of Sodium Foils. Unlike lithium metal foils, sodium foils are not commercially available and must be prepared in-house. The preparation steps are shown in Figure S21. Once the oxidized layer of the oil coated as-received sodium sticks is cut, pure shiny sodium metal is visible in the inner layers. A small portion is then cut away, cleaned briefly in a hexane solution, and then dried immediately. The cleaned sodium metal portion is then made into a thin foil by using a roller and then cut into desired shapes for use in the preparation of the coin cells.

2.8. Electrochemical Characterization and Analysis. The sodium-ion conductivities of the various prepared electrolytes were assessed using an electrochemical impedance spectroscopy (EIS) technique. A rhd measuring cell TSC battery (as shown in Figure S16) manufactured by rhd instruments GmbH & Co. KG with stainless-steel electrodes, which also acts as a current collector, was used for EIS experiments. The electrolytes cut into an 8 mm diameter were placed in between the stainless-steel electrodes. The EIS recordings were made between the set frequency ranges from 10^{-1} to 10^6 Hz, with a sinusoidal potential perturbation of 10 mV, and the spectra were obtained using a Zahner Zennium potentiostat using a four-point electrode cell.

The sodium-ion transference numbers of the prepared electrolytes were assessed by the AC-DC (alternating current-direct current) polarization technique using the prepared symmetrical cells Na||

electrolyte||Na (as shown in Figure S22). Initially, an AC polarization voltage of 10 mV was applied to the cell the EIS spectrum was recorded in the frequency range of 10^{-1} – 10^6 Hz, and the initial resistance (R_0) was calculated from the Nyquist plots. Then, a potentiostatic polarization or a DC polarization voltage of 10 mV was applied, and the current evolution (chronoamperogram) was recorded until a steady state was reached; afterward, the polarization was stopped, and the initial current (I_0) and the steady-state current (I_{SS}) were noted. Finally, another EIS spectrum was recorded, and the steady-state resistance (R_{SS}) was calculated from the Nyquist plots.⁶¹

The electrochemical stability window (ESW) of the prepared electrolytes was analyzed by linear sweep voltammetry (LSV) using a GAMRY potentiostat. For this purpose, the cells were assembled in an asymmetric configuration with a stainless-steel (SS) electrode and a Na foil counter electrode, i.e., SS||Electrolyte||Na configuration (as shown in Figure S22). The LSV was performed by conducting a positive scan from 2.5 to 6.5 V and a negative scan from 2.5 to 0 V, with a scan rate of 1 mV s^{-1} at 60 °C.

The symmetrical cells for both the pure polymer electrolyte (PEO-NaClO₄) and the fiber-reinforced structural electrolyte (GF_PEO-NZSP-NaClO₄) were prepared in the 2032 coin-cell configuration. The electrolyte membrane was sandwiched between two sodium foils (as shown in Figure S22). In total, two different symmetrical cells in the form Na||Electrolyte||Na were assembled for testing.

2.9. Structural Battery Half-Cell Assembly and Testing. The structural battery Na | GF_PEO-NZSP-NaClO₄ ||CF with a carbon fiber as a positive electrode and a sodium foil as a counter electrode was fabricated and tested in the 2032 coin-cell configuration. The coin-cell assembly is described in Figure S25. The prepared structural electrode with a diameter of 10 mm was placed above the spring and stainless-steel spacer in the coin-cell case, with the carbon fiber electrode facing the spacer, and then the prepared sodium foil (with a diameter of 13 mm) was attached to the structural electrolyte layer

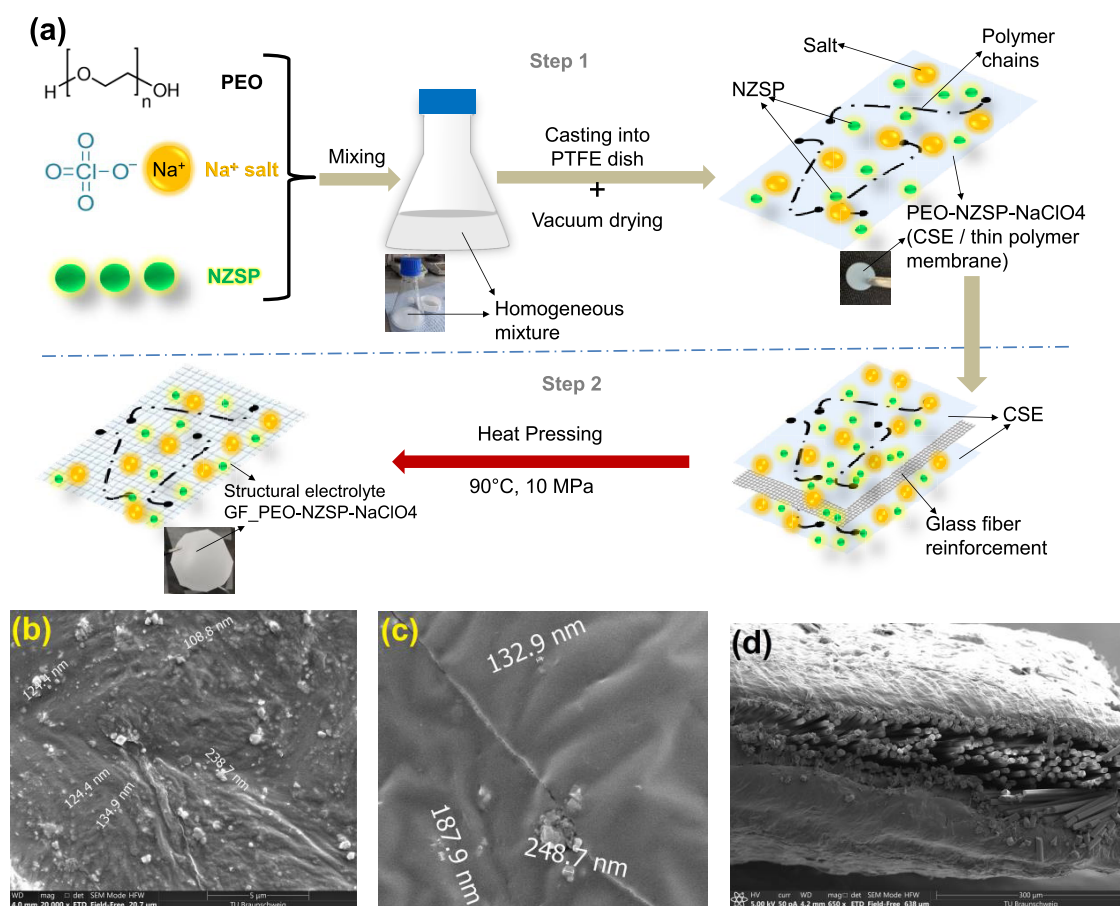


Figure 4. (a) Schematic showing the structural electrolyte preparation. SEM images: (b) Polymer nanocomposite PEO-NZSP-NaClO₄ surface showing embedded nanoparticles. (c) Structural electrolyte GF_PEO-NZSP-NaClO₄ surface. (d) Cross-sectional view of the structural electrolyte showing glass fibers sandwiched between two thin polymer electrolyte membranes.

(the layer which is attached to the carbon fiber electrode); the coin cell was then sealed inside a glovebox using an MTI MSK-160E pressure adjustable electric crimper (manufactured by MTI Corporation, California). The galvanostatic charging–discharging of the assembled structural battery was performed using a potentiostat (Reference 3000, Gamry LCC) and a special GAMRY dual 2032 coin-cell battery holder (Part number: 992000159). All of the above-mentioned procedures are done in a strict protective environment with humidity of 0 ppm and oxygen of 0 ppm. The capacities of the structural battery were calculated based on the aerial weight of the carbon fibers used, which is 55 g m⁻².

2.10. Mechanical Characterization. To assess the mechanical strength of the prepared thin polymer membranes, structural electrode, and electrolyte, tensile tests were performed in the Zwick-Roell universal testing machine (UTM) with a high-end GOM ARAMIS 3D industrial camera setup for precise, contactless strain measurements on the surface of the samples (as shown in Figure S9). The samples were covered with a specific paint in a speckle pattern, which gives a stochastic black and white pixel distribution on the sample surface that helps in precise elongation measurements. The samples were prepared according to the ASTM D-638 Type V standard, and the loading rate was set at 2 mm min⁻¹.

3. RESULTS AND DISCUSSION

3.1. Nanoparticle Characterization and Microstructure Analyses of the Structural Electrolyte and the Structural Electrode. The NASICON-type NZSP inorganic filler was first suggested by Goodenough, and it showed high ionic conductivity at room temperature.^{55,56} The chemical 3D structure of NZSP in the rhombohedral phase is shown in

Figure 3a. It has two corners sharing the tetrahedra, namely, [SiO₄] and [PO₄], one octahedra [ZrO₆], and two distinct sodium sites Na1 and Na2.⁵⁷ The Na2 site accommodates 3 mol Na⁺ ions, which helps in diffusion of ions contributing to high ionic conductivity.

The active NASICON-type Na₃Zr₂Si₂PO₁₂ (NZSP) nanoparticle fillers were added to enhance both Na⁺-ion conductivity and also to prohibit sodium dendrite formation through the polymer matrix. Before using the NZSP powder, it must be ground into pure nanoparticles with less agglomeration and characterized for their particle size so that it will be able to spread out evenly throughout the polymer matrix and aid in boosting sodium-ion conductivity.

The as-received NZSP (Na₃Zr₂Si₂PO₁₂) powder was wet ball-milled using a Fritsch planetary ball mill (Type: Pulverisette 7, manufactured by FRITSCH GmbH, Germany). Pure NZSP nanoparticles were obtained following the procedure elaborated in Section 2. The size distribution of the Na₃Zr₂Si₂PO₁₂ nanoparticles was analyzed using the centrifuge particle sizing (CPS) analyzer (Model: DC24000, manufactured by CPS Instruments, Europe). Three nanoparticle samples were prepared for analysis named NZSP_01, NZSP_02, and NZSP_03.

The procedure for CPS analysis is detailed in Section 2. As can be seen from the obtained normalized weight distribution plot shown in Figure 3b, the particle size distribution density of the majority of the nanoparticles is in the range less than 0.1 μm. The cumulative and absolute weight distribution plots

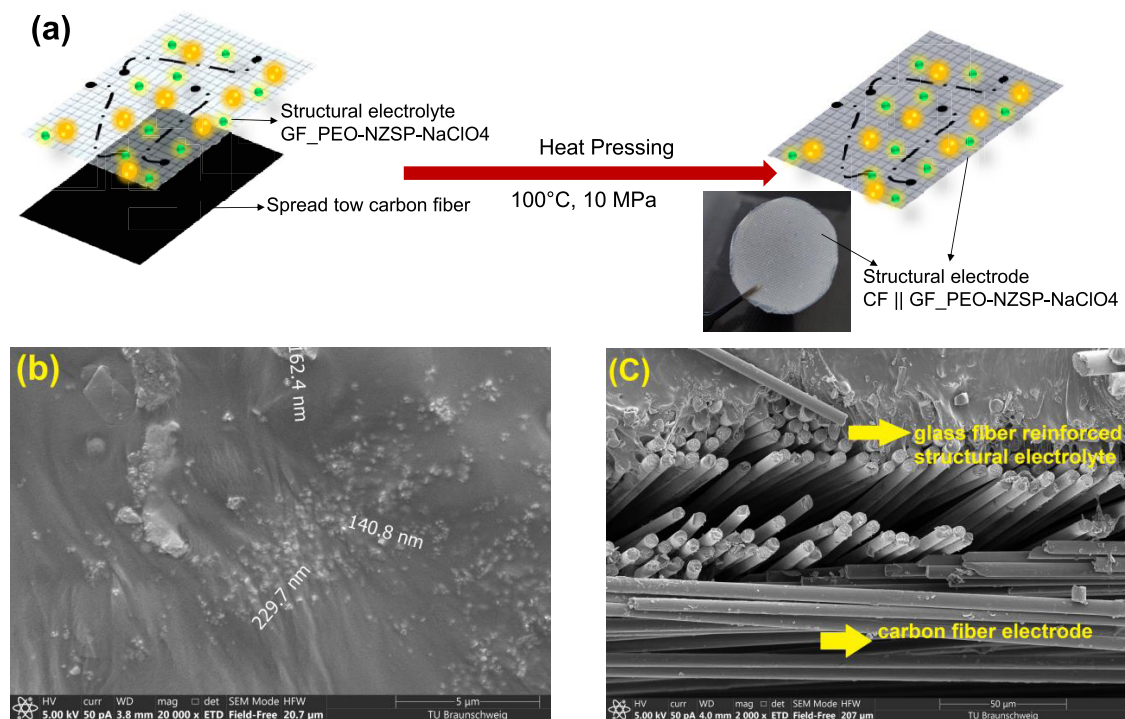


Figure 5. (a) Schematic showing the structural electrode preparation. SEM images: (b) Top view showing the surface of the carbon fiber-reinforced structural electrode. (c) Cross-sectional view showing carbon fiber reinforcement in the structural electrode beneath the structural electrolyte surface.

(Figure S2) from the CPS analysis also show similar particle size concentrations. The high-resolution SEM image obtained from the FEI scanning electron microscope, as shown in Figure 3c, confirms the size distribution of the nanoparticles, which is in the range of 11–300 nm.

The structural electrolytes were prepared using the process chain (Figure S3) described in Section 2. The schematic (Figure 4a) shows the chemicals used and the slurry casting procedure for production of the thin polymer membrane or a composite solid electrolyte (CSE), shown in Step 1, and the structural electrolyte (Step 2). Initially, certain amounts of the PEO powder and NaClO_4 salt were dissolved in the acetonitrile (ACN) solution, to which various amounts of NZSP nanoparticles were added and mixed until a homogeneous slurry mixture was obtained. This mixture was cast onto a PTFE dish and then vacuum-dried to get thin polymer membranes. The $\text{EO}:\text{Na}^+$ ratio was maintained at 15:1, as established in the recent PEO-based electrolyte studies.^{58,59} The process and the preparation are detailed in Section 2.

The composite solid electrolyte (CSE) with nanoparticles is identified as PEO-NZSP-NaClO_4 and that without nanoparticles is identified as PEO-NaClO_4 (Figure S4). The main structural electrolyte is prepared by heat pressing (using Collins P500S press, COLLIN Lab & Pilot Solutions GmbH Maitenbeth, Germany) a glass fiber woven fabric sandwiched between two PEO-NZSP-NaClO_4 membranes and is identified as $\text{GF_PEO-NZSP-NaClO}_4$ (Figure S4). For comparison, structural electrolytes are also prepared without nanoparticles and are identified as GF_PEO-NaClO_4 (Figure S4).

The CSE or thin polymer electrolyte membrane with NZSP nanoparticles had a thickness of around 180 μm , while the structural electrolyte had a thickness of 420 μm . The scanning electron microscopy (SEM) images, as shown in Figure 4b,4c,

show the distribution of nanoparticles on the CSE surface and the structural electrolyte surface, respectively. The SEM image in Figure 4d shows a cross-sectional view of the structural electrolyte, where the glass fiber sandwiched between two thin polymer membranes can be seen. The structural electrolyte remained stable during the heat press preparation process. The energy dispersive X-ray analysis (EDAX) SEM images of NZSP nanoparticles are shown in Figure S7, and a similar pattern can be observed in Figure S8, which confirms the presence of NZSP nanoparticles on the structural electrolyte surface, while Figure S8 also shows a portion of the exposed surface to X-rays. To test the shape durability of the structural electrolyte, it was heated to 160 $^\circ\text{C}$ for 35 min, and it retained shape even at high temperatures since the glass fibers absorb melted PEO through the capillary effect and hence ensure shape durability (Figure S5). In contrast, PEO-NaClO_4 was heated to 160 $^\circ\text{C}$ for 12 min, it melted, and its shape got deformed (Figure S5). Figure 5a shows the structural electrode preparation process. The as-received IMS 65 intermediate-modulus (IM) spread tow carbon fibers (CFs) were heat-pressed with the already prepared structural electrolyte to obtain the CF-laminated structural electrode. The PEO-based structural electrolyte acts as an adhesive, and the CF layer firmly holds onto it (Figure S6).

Figure 5b shows the SEM image of the surface of the structural electrode, and Figure 5c shows the cross-sectional view of the structural electrode showing the reinforced carbon fibers beneath the structural electrolyte. Figure S6 shows the upper and lower surfaces of the prepared structural electrode. The carbon fiber surface acts as an electrode and also as a current collector, simultaneously enhancing the overall mechanical properties.

3.2. Mechanical Characterization of the Thin Polymer Membrane, the Structural Electrolyte, and the Struc-

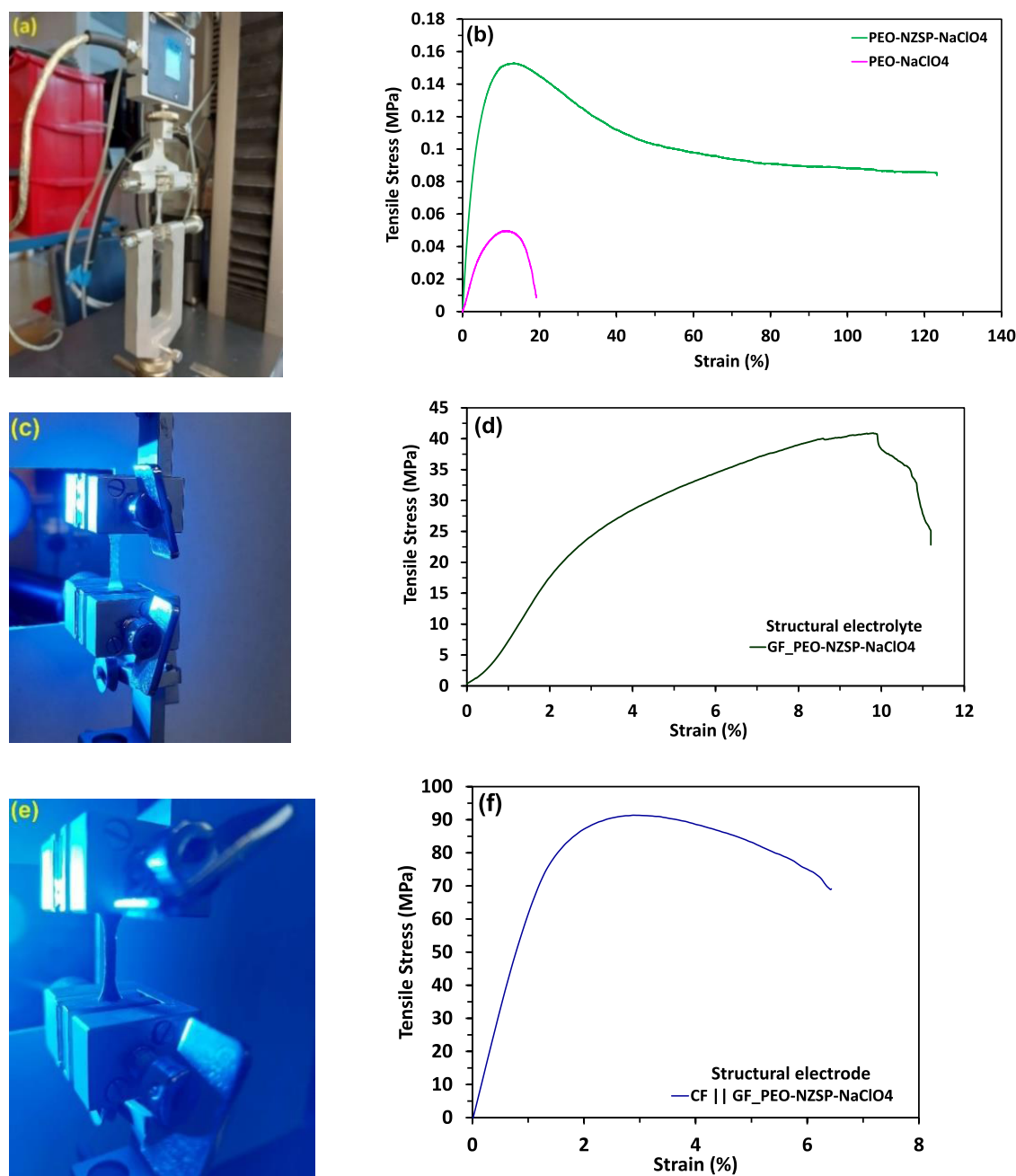


Figure 6. Mechanical characterization: (a) Experimental setup for the tensile test of thin polymer membranes. (b) Typical stress–strain curves of PEO-NaClO₄ and PEO-NZSP-NaClO₄ thin polymer composite membranes. (c) Experimental setup for the tensile test of structural electrolytes. (d) Typical stress–strain curve of structural electrolyte GF_PEO-NZSP-NaClO₄. (e) Experimental setup for the tensile test of structural electrodes. (f) Typical stress–strain curve of structural electrode CF||GF_PEO-NZSP-NaClO₄.

tural Electrode. As mentioned in Section 1, to achieve multifunctionality, every single component of a structural battery was modified so that it could store energy and as well provide sufficient structural strength. For this reason, the mechanical performance of the thin polymer membranes, the structural electrolyte, and the structural electrode were evaluated by tensile testing. The different sample types are shown in Figure S10. For statistical reasons, five samples of each type were tested according to the ASTM D-638 Type V standard.⁶⁰ The procedure and the experimental setup are discussed in Section 2.

The mechanical performance of the thin polymer membranes was evaluated by using a 10 N strain gauge/load cell

(using static material testing machine, ZwickRoell GmbH & Co. KG, Germany), and the experimental setup is shown in Figure 6a. The PEO-NaClO₄ membrane showed a tensile strength of 0.05 MPa with Young's modulus of 0.55 MPa, while PEO-NZSP-NaClO₄ showed a tensile strength of 0.15 MPa with Young's modulus of 4.25 MPa (Figure 6b). The PEO-NZSP-NaClO₄ membrane showed 3 times more tensile strength compared to the PEO-NaClO₄ membrane and appeared to be more tensile, as shown in Figure S11. This can be attributed to the addition of nanoparticles, which enhance the mechanical properties of the PEO-NZSP-NaClO₄ membranes. The force–displacement curves for the thin polymer membrane are shown in Figure S14. The calculated

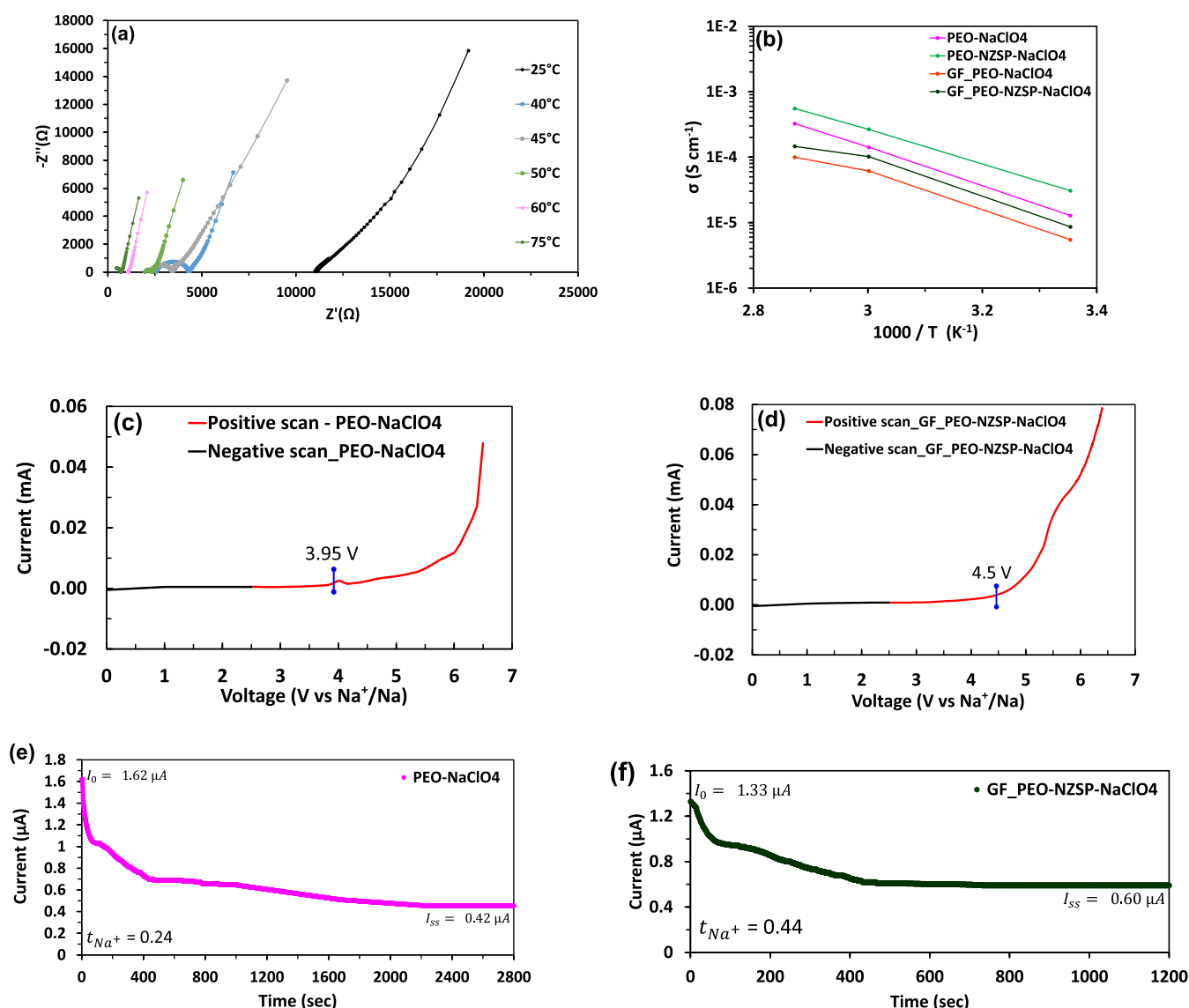


Figure 7. Electrochemical characterization: (a) EIS of structural electrolyte GF_PEO-NZSP-NaClO₄ at different temperatures. (b) Ionic conductivities of various electrolytes from 25 to 75 °C. (c) Linear sweep voltammetry (LSV) curves of the PEO-NaClO₄ membrane. (d) Linear sweep voltammetry (LSV) curves of structural electrolyte GF_PEO-NZSP-NaClO₄. (e) Chronoamperogram or current response and EIS of the Na||PEO-NaClO₄||Na symmetrical cell to applied dc polarization. (f) Chronoamperogram or current response and EIS of the Na||GF_PEO-NZSP-NaClO₄||Na symmetrical cell to applied dc polarization.

mean and standard deviation values for the PEO-NaClO₄ samples are 0.0518 and 0.0023 MPa, respectively, while for the PEO-NZSP-NaClO₄ samples, they are 0.1447 and 0.0121 MPa, respectively (Figure S15).

The tensile test setup using a 5 kN strain gauge/load cell and the typical stress–strain curve for the mechanical performance of the structural electrolyte sample are shown in Figure 6c,6d, respectively. The obtained tensile strength is 40.9 MPa, which is more than 250 times greater compared to that of the thin polymer membranes, and this can be attributed to the glass fiber reinforcements, which had a positive influence on the overall strength. For the precise strain measurements, the GOM ARAMIS industrial camera was used, and the strain measurements from the start point and while under loading of the tensile test are shown in Figure S12. The calculated mean and standard deviation for the samples are 40.50 and 7.14 MPa, respectively (Figure S15). Young's modulus was

calculated to be 1.42 GPa. The force–displacement curves for the structural electrolyte are shown in Figure S14.

Figure 6e shows the experimental setup using the 5 kN load cell/strain gauge, and the typical stress–strain curve for the tested structural electrolyte sample is shown in Figure 6f. The material offers a tensile strength of 91.3 MPa. Figure S13 shows the strain measurements from the start point and while under loading of the sample, and the Young's modulus was calculated to be 2.7 GPa. This increase in tensile strength can be attributed to the addition of a high tensile strength single carbon fiber layer to the structural electrolyte. Figure S14 shows the force–displacement curves of the different structural electrolyte samples.

The calculated mean and standard deviation for the samples are 89.58 and 17.47 MPa, respectively, as shown in Figure S15.

3.3. Electrochemical Characterization of Structural Electrolytes. The prepared electrolytes were evaluated for their sodium-ion conductivities, electrochemical stability

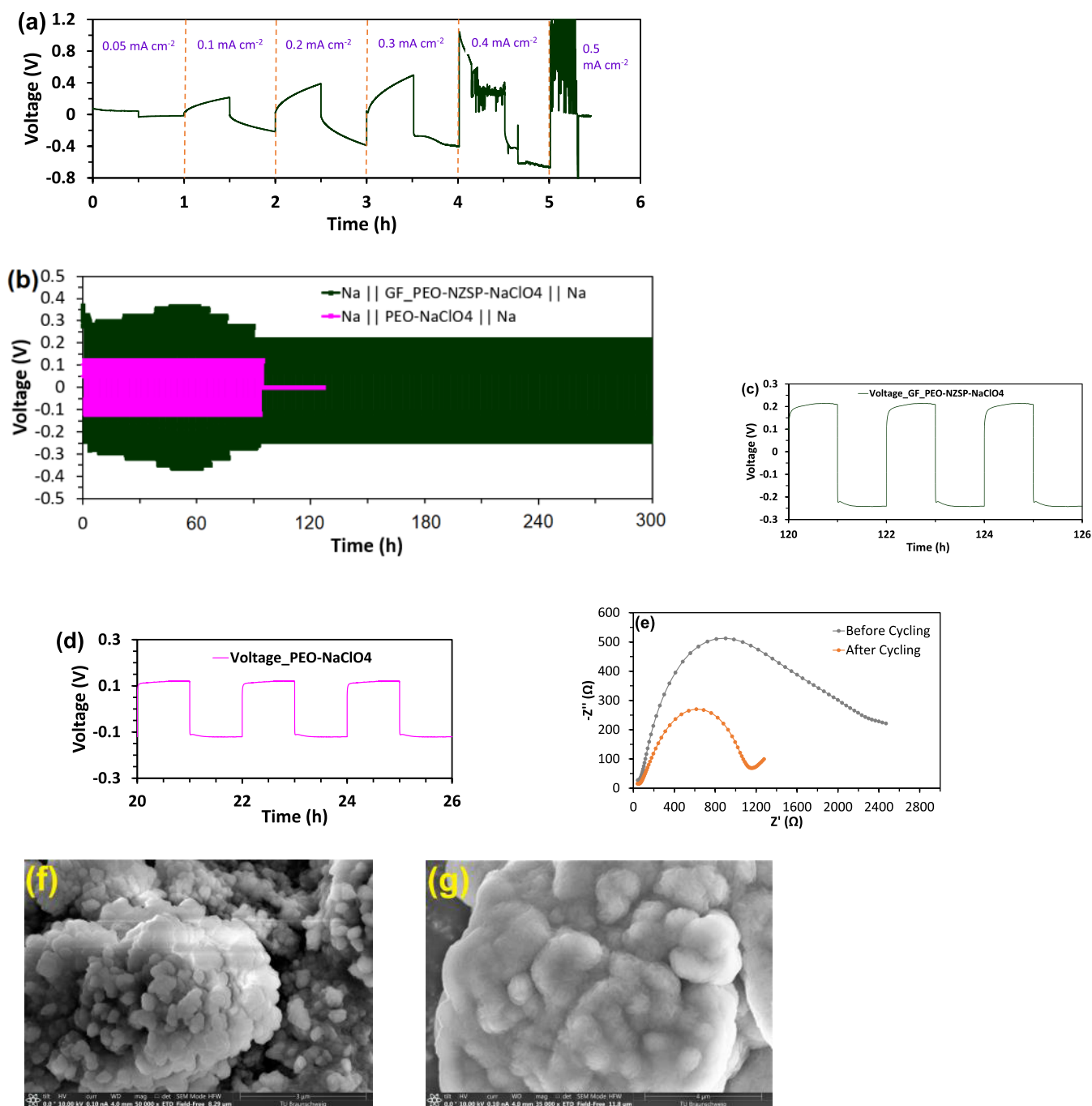


Figure 8. (a) Galvanostatic cycling curves with varying current densities for the symmetric cell Na||GF_PEO-NZSP-NaClO₄||Na at 60 °C. (b) Galvanostatic cycling of symmetrical cells Na||GF_PEO-NZSP-NaClO₄||Na and Na||PEO-NaClO₄||Na for a current density of 0.1 mA cm⁻² at 60 °C. (c) Typical voltage profile of the Na||GF_PEO-NZSP-NaClO₄||Na cell from 120 to 126 h. (d) Typical voltage profile of the Na||PEO-NaClO₄||Na cell from 20 to 26 h. (e) EIS of Na||GF_PEO-NZSP-NaClO₄||Na symmetrical cells before and after cycling. (f) SEM image of the Na electrode for the Na||PEO-NaClO₄||Na cell after cycling. (g) SEM image of the Na electrode for the Na||GF_PEO-NZSP-NaClO₄||Na cell after cycling.

window, ion transference, sodium dendrite growth inhibition, and cycling stability, which are critical for their use in structural battery applications. The sodium-ion conductivities of the prepared electrolytes were evaluated using the electrochemical impedance spectroscopy (EIS) technique, which is detailed in Section 2.

The ionic conductivities (σ) are evaluated from the Nyquist plots (Figures 7a and S18) by using the obtained bulk resistances (R_L). The value of the bulk resistance (R_L) of the electrolytes can be calculated either using the EIS equivalent

circuit (as shown in Figure S17) or from the Nyquist plot, where the semicircles at high frequencies meet the real axis. The ionic conductivity was then calculated using eq 1.

$$\sigma = \frac{t}{AR_L} \quad (1)$$

where t is the thickness of the electrolyte and A is the geometric area that is in contact with the stainless-steel electrodes.

Among the various prepared composite solid electrolytes (CSE) with different weight ratios of NZSP nanoparticles, the glass-fiber-reinforced structural electrolytes were prepared using CSE with 25% by weight NZSP nanoparticles, which showed the maximum ionic conductivity of $2.4 \times 10^{-5} \text{ S cm}^{-1}$ at 25 °C (as shown in Figure S18), which is comparable to the values reported in the previous study.⁵⁹ The decrease in ionic conductivity beyond 30% by weight NZSP is due to the agglomeration of the nanoparticles, which leads to uneven distribution in the polymer matrix. The EIS Nyquist plots comparison of the electrolytes PEO-NaClO₄, GF_PEO-NaClO₄ (without NP), and GF_PEO-NZSP-NaClO₄ (with NP) at 25 °C are shown in Figure S18. The ionic conductivity of structural electrolyte GF_PEO-NZSP-NaClO₄ was found to be less than PEO-NaClO₄ at $8.58 \times 10^{-6} \text{ S cm}^{-1}$ at 25 °C, which is largely due to the insulative behavior of glass fibers sandwiched between the two CSE layers, although it is still much greater than the structural electrolyte without NZSP nanoparticle fillers (GF_PEO-NaClO₄). The addition of nanoparticles in the electrolyte creates vacancies in the structure, and using these vacant sites, Na⁺-ion diffusion takes place, boosting the ionic conductivity.⁵⁵ This is typical for ion conduction in solid-state electrolytes, and the PEO polymer provides pathways for ion conduction.

Figure 7a shows the Nyquist plot of structural electrolyte GF_PEO-NZSP-NaClO₄ at different temperatures. At and above a temperature of 60 °C, it showed an acceptable ionic conductivity of $1.02 \times 10^{-4} \text{ S cm}^{-1}$, essential for improved battery operation. The temperature-induced behavior of the ionic conductivity is shown in Figure 7b for various electrolytes. The Arrhenius plot for the electrolytes is shown in Figure S19. The ionic conductivities at different temperatures for all of the prepared electrolytes are summarized in Figure S20.

The electrochemical stability window (ESW) of the prepared electrolytes was evaluated by linear sweep voltammetry (LSV) measurements using asymmetric cells (SS||electrolyte||Na). The experiment was performed by conducting positive and negative scans from 2.5 to 6.5 V and from 2.5 to 0 V, respectively, with a scan rate of 1 mV s^{-1} at 60 °C. The obtained LSV curves for PEO-NaClO₄ and structural electrolyte GF_PEO-NZSP-NaClO₄ are shown in Figure 7c,7d, respectively. The current for the applied potential drop across the electrolyte is observed, and the ESW is determined as the upper limit voltage at which there is a peak or dip in current values from the obtained LSV plots. The ESW of PEO-NaClO₄ is 3.95 V, while that of GF_PEO-NZSP-NaClO₄ is 4.5 V. The ESW of PEO-NZSP-NaClO₄ and GF_PEO-NaClO₄ is, respectively, 4.06 and 4.2 V (as shown in Figure S23). This shows that the addition of active nanoparticles NZSP and GF broadened the ESW, which can be attributed to their stabilization effects.³⁴

The transference ion number of the electrolytes was measured with the symmetrical cell configuration (N||Electrolyte||Na) using the alternating current (ac)–direct current (dc) experiments, explained in detail in Section 2. The current response or the chronoamperogram (for the applied dc polarization V) recorded for the N||PEO-NaClO₄||Na symmetric cell and structural electrolyte symmetric cell N||GF_PEO-NZSP-NaClO₄||Na are shown in Figure 7e,7f, respectively. The initial current (I_0) and the steady-state current (I_{ss}) were obtained from the dc experiment. The recorded EIS spectrum (for ac polarization) before and after

the current response is shown in Figure S24. The initial resistance (R_0) and the steady-state resistance (R_{ss}) were calculated from the ac experiment using EIS Nyquist plots. The transference ion number was then calculated using eq 2.⁶¹

$$t_{\text{Na}^+} = \frac{I_{ss}(\Delta V - I_0 R_0)}{I_0(\Delta V - I_{ss} R_{ss})} \quad (2)$$

The calculated sodium-ion transference number of the structural electrolyte GF_PEO-NZSP-NaClO₄ was 0.44 and for PEO-NaClO₄ it was 0.24 at 60 °C, which is comparable to the values reported in the literature.⁶² The high sodium-ion transference numbers for the structural electrolyte show the effect of addition of sodium-rich NZSP nanoparticle fillers and also the ability of glass fibers to boost the movement of Na⁺ ions.³³

To investigate the sodium dendrite inhibition capability of the structural electrolyte, a symmetrical cell configuration (N||GF_PEO-NZSP-NaClO₄||Na) was used, and galvanostatic cycling was performed at 60 °C by gradually increasing current densities.

The charging and discharging cycles were performed for 0.5 h for each current density, and the obtained curves are shown in Figure 8a. It can be seen that at a current density of 0.4 mA cm⁻², the short circuit begins, indicating the sodium dendrite formation through the polymer matrix layers. Hence, the critical charge density (CCD) for the structural electrolyte is found to be 0.4 mA cm⁻², beyond which the sodium dendrite inhibition capability fails. To evaluate the cycling stability and performance of the structural electrolyte GF_PEO-NZSP-NaClO₄, again, a symmetric cell configuration (N||GF_PEO-NZSP-NaClO₄||Na) was used, and galvanostatic cycling was performed for a constant current density of 0.1 mA cm⁻². For comparison, galvanostatic cycling was also performed with a symmetrical cell (N||PEO-NaClO₄||Na). The galvanostatic cycling curves for both symmetrical cells are plotted, as shown in Figure 8b. The structural electrolyte GF_PEO-NZSP-NaClO₄ ran smoothly for 300 h, while PEO-NaClO₄ performed for only 90 h before it stopped. This indicates the formation of sodium dendrites sooner in the polymer membrane PEO-NaClO₄, which effectively short-circuits the cell.

The stability of the structural electrolyte GF_PEO-NZSP-NaClO₄ can be attributed to the ability of NZSP nanoparticles to suppress the growth of sodium dendrites, thereby avoiding a short circuit of the cell. Figure 8c shows the typical voltage profile of GF_PEO-NZSP-NaClO₄ from 120 to 126 h, while Figure 8d shows the typical voltage profile of PEO-NaClO₄ from 20 to 26 h. From the EIS Nyquist plot (Figure 8e), the interfacial resistance for the N||GF_PEO-NZSP-NaClO₄||Na symmetrical cell before and after cycling was found to be 2038 and 1100 Ω, respectively, which explains the initial increase in voltage for the structural electrolyte symmetrical cell N||GF_PEO-NZSP-NaClO₄||Na, and it settled down around the 90th cycle and then provided a smooth voltage profile. This initial high resistance can be attributed to the bad interface because of side reactions of NZSP nanoparticles with sodium metal and also due to the sodium plating process, leading to local sodium dendrite formation.^{63–65} Once the interface is stabilized, with the ability of NZSP active nanoparticle fillers to suppress the dendrite formation, the voltage is decreased, and a smooth voltage profile, as shown in Figure 8c, is obtained after 90 h. Figure 8f,8g shows the SEM images of the Na electrode

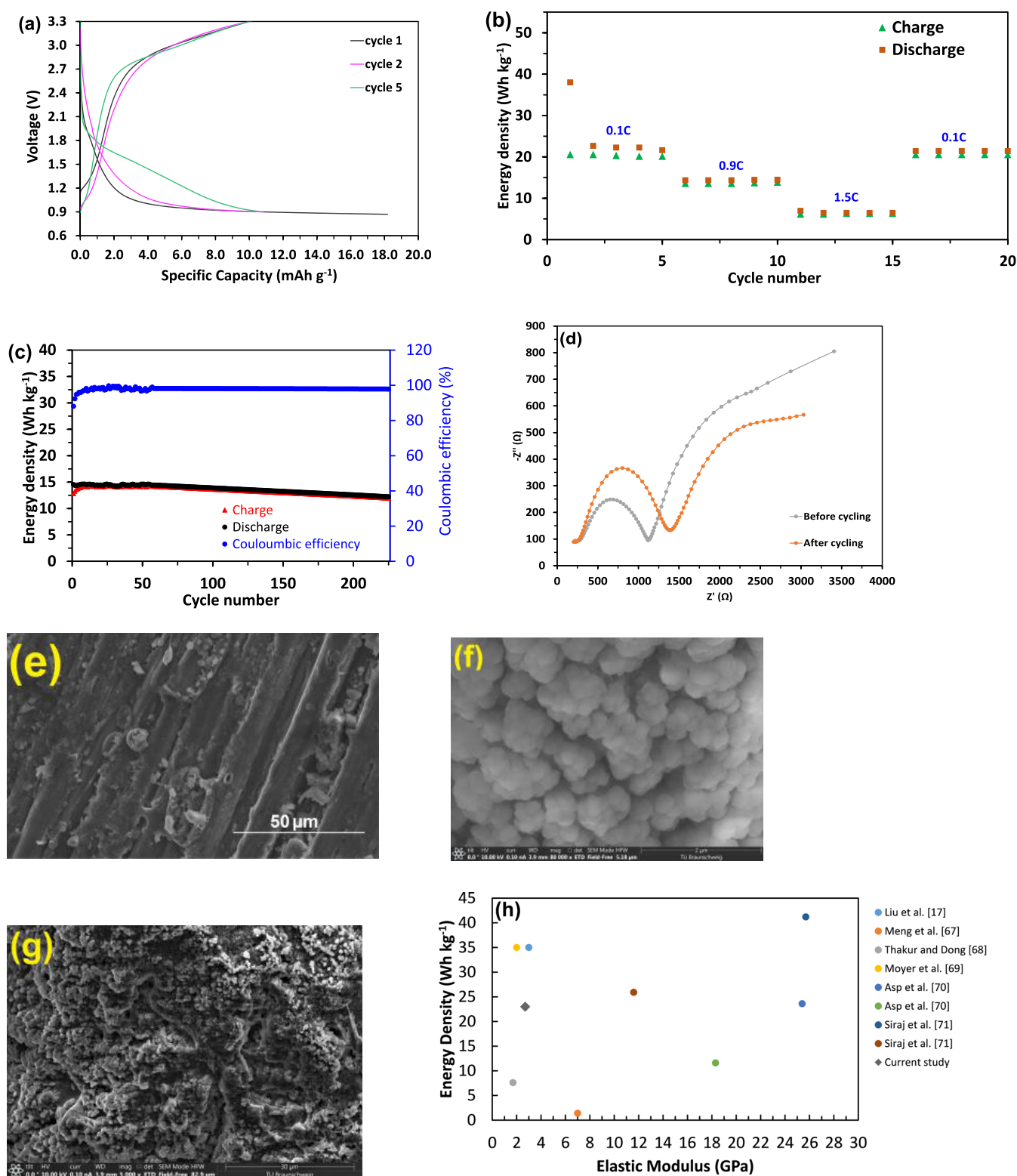


Figure 9. Structural battery performance: (a) Charge–discharge profiles of the CF||GF_PEO-NZSP-NaClO₄||Na cell for the 0.1C rate. (b) Rate capability tests showing specific capacity vs. cycle number of the CF||GF_PEO-NZSP-NaClO₄||Na cell at different C rates. (c) Stability tests showing charge–discharge energy density and Coulombic efficiency vs. cycle number of the CF||GF_PEO-NZSP-NaClO₄||Na cell for the 0.9C rate. (d) EIS of the CF||GF_PEO-NZSP-NaClO₄||Na cell before and after cycling. (e) SEM image of the carbon fiber electrode after cycling. (f) SEM image of the Na electrode after cycling. (g) SEM image showing the SEI layer formed above the carbon fiber electrode surface after cycling. (h) Reported cell level energy densities and elastic modulus of various structural batteries with literature references.

of Na||PEO-NaClO₄||Na and Na||GF_PEO-NZSP-NaClO₄||Na

symmetrical cells after cycling, respectively.

3.4. Structural Battery Performance and Characterization. The structural battery was fabricated with the as-received spread tow carbon fibers (CFs) as a cathode and

Table 1. Table Showing the Fabrication Technique, Electrolyte Type, Ion Type, Energy Densities, and Specific Capacities of Various Structural Battery Cells Reported in the Literature

references	electrolyte type	structural battery fabrication technique	ion type	reported values		
				C rate	specific capacity (Ah kg ⁻¹)	energy density (Wh kg ⁻¹)
Liu et al. ¹⁷	gel–polymer-type electrolyte	lamination of carbon fibers to electrolytes	Li ion	0.05C	DNA ^a	35
Meng et al. ⁶⁷	Kevlar reinforced gel-type electrolyte	use of heterogeneous material interfaces using carbon nanotubes	Li ion	DNA ^a	DNA ^a	1.4
Thakur and Dong ⁶⁸	solid-polymer-type electrolyte coated on individual carbon fibers	multiaxis coextrusion deposition	Li ion	0.5C	23.4	7.6
Moyer et al. ⁶⁹	liquid electrolyte impregnated on the Celgard separator	vacuum infusion of the electrolyte	Li ion	0.1C	30	35
Asp et al. ⁷⁰	bicontinuous-phase-type electrolyte with a GF plain weave separator	thermal curing after electrolyte impregnation	Li ion	0.05C	8.55	23.6
Asp et al. ⁷⁰	bicontinuous-phase-type electrolyte with a Whatman GF/A separator	thermal curing after electrolyte impregnation	Li ion	0.05C	4.13	11.6
Siraj et al. ⁷¹	bicontinuous-phase-type electrolyte with a GF plain weave separator	thermal curing after electrolyte impregnation	Li ion	0.05C	14.7	41.2
Siraj et al. ⁷¹	bicontinuous-phase-type electrolyte with a Whatman GF/A separator	thermal curing after electrolyte impregnation	Li ion	0.05C	9.82	25.9
Danzi et al. ⁴⁴	all-solid-state ferroelectric Na _{2.99} Ba _{0.005} ClO electrolyte	coaxial design using CFRP with a copper foil as a cathode and a coaxial aluminum rod as an anode	Na ion	DNA ^a	41.0	38
Valente et al. ⁴⁵	all-solid-state ferroelectric Na _{2.99} Ba _{0.005} ClO electrolyte	coaxial design using CFRP with a cork/copper foil as a cathode and a coaxial aluminum rod as an anode	Na ion	DNA ^a	110 ^b	99 ^c
this work	all-solid-state composite structural electrolyte embedded with a glass fiber woven fabric separator	solution casting (Step 1) followed by heat pressing (Step 2) under high pressure and temperature	Na ion	0.1C	10.8	23

^aData Not Available. ^bUnits are in mAh cm⁻². ^cUnits are in mWh cm⁻².

sodium metal as an anode (CF||GF_PEO-NZSP-NaClO₄||Na) in the form of 2032 coin cells, as shown in Figure S25. The procedure is detailed in Section 2. The charge–discharge profiles at a 0.1C rate are shown in Figure 9a. The cell was galvanostatically charged and discharged in the voltage range of 0.9–3.3 V. The average nominal voltage during discharge was 2.1 V, and the cell capacities were calculated based on the aerial weight of the carbon fibers (55 g m⁻²). It showed an initial high discharge capacity of 18 mAh g⁻¹ and a charge capacity of 9.8 mAh g⁻¹ for the first cycle. The discharge capacity suddenly changed to 10.8 mAh g⁻¹ in the second cycle, which can be attributed to the formation of stable solid electrode interface (SEI) layers, and subsequently, the Coulombic efficiency improved from the second cycle onward and reached 98%.⁶⁶ In the subsequent cycles, the discharge–charge capacities remained fairly constant, and the typical energy density at a 0.1C rate was calculated to be 22.7 Wh kg⁻¹. Figure 9b shows the rate capability plots for different C-rates, with 5 cycles for each rate. Energy densities of 22.7, 14.6, and 6.6 Wh kg⁻¹ were obtained for C-rates 0.1C, 0.9C, and 1.5C, respectively. The energy density drop at high current densities could be due to mass transport constraints, which also depends on the type of carbon fibers used. After the 15th cycle, again for the 0.1C rate, the energy densities remained fairly constant. These values are comparable to the energy densities reported for DOI III-type structural batteries in the literature, as shown in Table 1. The comparison is a bit skewed due to the different methodologies and fabrication techniques adopted by various researchers in the structural battery domain, but nevertheless, it gives a rough estimate of the energy density range of current DOI III structural battery designs, which is between 1 and 42 Wh kg⁻¹. The best chemistries to obtain structural batteries with further high

energy densities and fabrication methodologies remain an open research question.

The fabrication method used in this study provides a novel way to manufacture structural batteries in addition to the existing approaches. The cycling performance of the structural battery was investigated for a 0.9C rate, and the charge–discharge profiles and Coulombic efficiency versus cycle number are shown in Figure 9c. While the Coulombic efficiency was at 92% during the initiation process, where the polymer establishes firm contact with the carbon fiber electrodes, the cell capacity gradually increased, and the Coulombic efficiency eventually reached a high value of 98% after 20 cycles and remained consistent thereafter. The cell showed the ability to retain 80% capacity until 225 cycles, and overall, it performed 500 cycles with gradually degraded capacity retention, with 36% of initial capacity at the 500th cycle. The cell capacity retention versus cycle number plot is shown in Figure S26. This gradual capacity degradation can be attributed to the increased charge-transfer resistance (R_{ct}), as calculated from the EIS Nyquist plot shown in Figure 9d. Before cycling, the cell had a R_{ct} of 900 Ω, while at the end of 225 cycles, the R_{ct} increased to 1250 Ω due to sodium dendrite formation, which leads to capacity deterioration. Figure 9e,f shows the carbon fiber and Na electrodes after cycling, respectively. The excellent cycling stability obtained can be attributed to stable solid electrolyte interphase (SEI) layers, and the SEM image of the SEI layer is shown in Figure 9g. It is further characterized using EDAX, and the obtained pattern is shown in Figure S27. The EDAX pattern of the SEI layer shows that both the NZSP nanoparticles and the embedded glass fibers contribute to the cycling stability of the structural electrolyte. Figure 9h compares the various reported cell-level energy densities and elastic modulus combinations of the DOI

III-type structural batteries reported in the literature with the current study. The energy density reported in the current study is in the median range with respect to all reported DOI III structural batteries.

The electrochemical performance can be improved further by utilizing chemically treated carbon fibers. The Na⁺-ion intercalation onto carbon fiber microstructures can be further ameliorated using a special coating of electrode materials such as aerogels, carbon nanotubes (CNTs), 2D nanomaterials, etc., which requires further investigation. The carbon fiber (CF) density also plays an important role in the overall cell performance. With more fiber volume, by stacking carbon fiber layers, which is typical for structural batteries, both the electrochemical capacity and the overall structural strength are certainly further enhanced.¹³ The glass fibers though provided good structural strength and shape stability and contributed to cycling stability, they also had a negative impact on the ionic conductivity of the structural electrolyte; this can be further improved by replacing glass fibers with less insulative materials. The next steps in developing a full sodium-ion-based structural battery include using CF as an anode, replacing the Na metal electrode (used in this study), and testing it with carbon fiber electrodes coated with suitable sodium-rich cathode materials as the main source of Na⁺ ions. It can be represented as CF (with cathode coating)||structural electrolyte||CF (anode). The CF needs to be coated in an innovative way so as to function as a structural cathode and also as a current collector. Such a structural battery is expected to have more structural strength since CF is used also as an anode and needs to be characterized for its multifunctional performance.

4. CONCLUSIONS

This preliminary work developed sodium-ion-based structural battery components and investigated their multifunctional performance. The cell components revealed remarkable tensile strength and demonstrated sodium-ion insertion capabilities using untreated intermediate-modulus carbon fibers (as received) as electrodes with a high scope for improvements. The prepared structural electrolyte component using a high-strength glass fiber-reinforced poly(ethylene oxide)-based composite possessed multifunctional characteristic and showed a tensile strength of 40.9 MPa, an ionic conductivity of $1.02 \times 10^{-4} \text{ S cm}^{-1}$ at 60 °C, a sodium-ion transference number of 0.44, and an electrochemical stability window of 0 to 4.5 V. It also showed excellent cycling stability with sodium dendrite suppression capability. A structural electrode was made by laminating the structural electrolyte with the as-received intermediate-modulus spread with carbon fibers, which showed a high tensile strength of 91.3 MPa. Finally, structural cell CF||GF_PEO-NZSP-NaClO₄||Na was fabricated and tested for sodium-ion insertion capabilities with carbon fiber electrodes. It showed excellent cycling stability, with a typical energy density of 23 Wh kg⁻¹, and performed 500 cycles while retaining 80% capacity until 225 cycles. The structural battery architecture showed multifunctional performance that is necessary for the development of structural energy storage devices and systems.

■ ASSOCIATED CONTENT

SI Supporting Information

The Supporting Information is available free of charge at <https://pubs.acs.org/doi/10.1021/acsaem.4c00281>.

NZSP nanoparticle size distribution obtained using a centrifugal particle sizing analyzer; process chain for structural electrolyte preparation; images showing the prepared electrolytes; images showing the shape durability test on electrolytes at high temperatures; images showing the prepared electrodes; EDAX pattern of NZSP nanoparticles; EDAX pattern of the structural electrolyte surface; experimental setup for mechanical characterization; images of ASTM D-638 standard samples used for tensile testing; images showing tensile test strain measurements using an ARAMIS camera; force–displacement curves of electrolytes and electrodes; standard deviation plots obtained for the tensile test; EIS experimental setup; EIS equivalent circuit for electrolytes; EIS of different composite solid electrolytes at 25 °C; EIS of structural electrolytes at 25 °C; Arrhenius plot of all of the prepared electrolytes; plot showing ionic conductivity values for all prepared electrolytes at different temperatures; sodium-foil preparation process; coin-cell assembly schematic for asymmetric and symmetric cells; LSV curves of PEO-NZSP-NaClO₄ and GF_PEO-NaClO₄ electrolytes; EIS Nyquist plots from transference ion measurements before and after polarization; transference ion measurements; coin-cell assembly schematic for the structural battery; plot showing cell capacity retention versus cycle number for the investigated structural sodium battery; and EDAX pattern of the SEI (solid electrolyte interphase) layer on the electrode surface observed after structural battery cycling (PDF)

■ AUTHOR INFORMATION

Corresponding Author

Vasan Iyer – Cluster of Excellence SE2A—Sustainable and Energy Efficient Aviation, Technische Universität Braunschweig, 38108 Braunschweig, Germany; Institute of Lightweight Systems, Department of Multifunctional Materials, German Aerospace Center (DLR), 38108 Braunschweig, Germany; orcid.org/0000-0001-8868-6710; Email: vasan.iyer@dlr.de

Authors

Jan Petersen – Cluster of Excellence SE2A—Sustainable and Energy Efficient Aviation, Technische Universität Braunschweig, 38108 Braunschweig, Germany; Institute of Lightweight Systems, Department of Multifunctional Materials, German Aerospace Center (DLR), 38108 Braunschweig, Germany

Sebastian Geier – Cluster of Excellence SE2A—Sustainable and Energy Efficient Aviation, Technische Universität Braunschweig, 38108 Braunschweig, Germany; Institute of Lightweight Systems, Department of Multifunctional Materials, German Aerospace Center (DLR), 38108 Braunschweig, Germany

Peter Wierach – Cluster of Excellence SE2A—Sustainable and Energy Efficient Aviation, Technische Universität Braunschweig, 38108 Braunschweig, Germany; Institute of Lightweight Systems, Department of Multifunctional Materials, German Aerospace Center (DLR), 38108 Braunschweig, Germany; Institute of Polymer Materials and Plastics Engineering, Technische Universität Clausthal, 38678 Clausthal-Zellerfeld, Germany

Complete contact information is available at:
<https://pubs.acs.org/10.1021/acsaem.4c00281>

Notes

The authors declare no competing financial interest.

ACKNOWLEDGMENTS

The authors would like to acknowledge the funding by the Deutsche Forschungsgemeinschaft (DFG, German Research Foundation) under Germany's Excellence Strategy—EXC 2163/1—Sustainable and Energy Efficient Aviation—Project-ID 390881007. Furthermore, they also acknowledge support by the Open Access Publication Funds of the Technische Universität Braunschweig.

REFERENCES

- (1) European Commission. The European Green Deal 2024. <https://europa.eu/!DG37Qm>. (accessed January, 2024).
- (2) European Commission. Clean Sky Benefits 2024. <https://www.clean-aviation.eu/benefits-for-cleaner-greener-healthier-skies>. (accessed January, 2024).
- (3) NASA. NASA Aeronautics - Strategic Implementation Plan—2019 Update 2024. <https://www.nasa.gov/sites/default/files/atoms/files/sip-2019-v7-web.pdf>. (accessed January, 2024).
- (4) European Commission. Flightpath 2050 2024. <https://data.europa.eu/doi/10.2777/15458>. (accessed January, 2024).
- (5) The Cluster of Excellence SE²A—Sustainable and Energy-Efficient Aviation 2024. <https://www.tu-braunschweig.de/en/se2a>. (accessed January, 2024).
- (6) Thomas, J. P.; Qidwai, M. A. Mechanical design and performance of composite multifunctional materials. *Acta Mater.* **2004**, *52*, 2155–2164.
- (7) Wetzel, E. D. Reducing Weight: Multifunctional Composites Integrate Power, Communications, and Structure. *AMPTIAC Q.* **2004**, *8*, 91–95.
- (8) Adam, T. J.; Liao, G.; Petersen, J.; Geier, S.; Finke, B.; Wierach, P.; Kwade, A.; Wiedemann, M. Multifunctional Composites for Future Energy Storage in Aerospace Structures. *Energies* **2018**, *11*, No. 335.
- (9) Yu, Y.; Zhang, B.; Feng, M.; Qi, G.; Tian, F.; Feng, Q.; Yang, J.; Wang, S. Multifunctional structural lithium ion batteries based on carbon fiber reinforced plastic composites. *Compos. Sci. Technol.* **2017**, *147*, 62–70.
- (10) Johannisson, W.; Ihrner, N.; Zenkert, D.; Johansson, M.; Carlsted, D.; Asp, L. E.; Sieland, F. Multifunctional performance of a carbon fiber UD lamina electrode for structural batteries. *Compos. Sci. Technol.* **2018**, *168*, 81–87.
- (11) Ladpli, P.; Nardari, R.; Kopsaftopoulos, F.; Wang, Y.; Chang, F.-K. In *Design of Multifunctional Structural Batteries with Health Monitoring Capabilities*; Proceedings of the 8th European Workshop on Structural Health Monitoring (EWSHM 2016); Bilbao: Spain, 2016.
- (12) Thomas, J. P.; Qidwai, W. R.; Pogue, W. R., III; Pham, G. Multifunctional structure battery composites for marine systems. *J. Compos. Mater.* **2013**, *47*, 5–26.
- (13) Mullenax, J.; Browning, P.; Huebsch, W.; Gautam, M.; Sabolsky, E. M. In *Composite Multifunctional Lithium-Ion Batteries in ECS Trans*, Proceedings of the 220th Electrochemical Society (ECS) Meeting; Sunkara, M.; Abraham, K.; Smart, M.; Brodd, R.; Bugga, R., Eds.; The Electrochemical Society: Pennington, NJ, USA, 2012; pp 175–185.
- (14) Pereira, T.; Guo, Z.; Nieh, S.; Arias, J.; Hahn, T. Embedding thin-film lithium energy cells in structural composites. *Compos. Sci. Technol.* **2008**, *68*, 1935–1941.
- (15) Petersen, J.; Kube, A.; Geier, S.; Wierach, P. Structure-Integrated Thin-Film Supercapacitor as a Sensor. *Sensors* **2022**, *22*, No. 6932.
- (16) Wong, E. L.; Baechele, D. M.; Xu, K.; Carter, R. H.; Snyder, J. F.; Wetzel, E. D. In *Design and Processing of Structural Composite Batteries*, Proceedings of the Society for the Advancement of Material and Process Engineering (SAMPE); Baltimore: MD, USA, 2007.
- (17) Liu, P.; Sherman, E.; Jacobsen, A. Design and fabrication of multifunctional structural batteries. *J. Power Sources* **2009**, *189*, 646–650.
- (18) Lee, J. K.; An, K. W.; Ju, J. B.; Cho, B. W.; Cho, W. I.; Park, D.; Yun, K. S. Electrochemical properties of PAN-based carbon fibers as anodes for rechargeable lithium ion batteries. *Carbon* **2001**, *39*, 1299–1305.
- (19) Kjell, M. H.; Jacques, E.; Zenkert, D.; Behm, M.; Lindbergh, G. PAN-Based Carbon Fiber Negative Electrodes for Structural Lithium-Ion Batteries. *J. Electrochem. Soc.* **2011**, *158*, A1455–A1460.
- (20) Jacques, E.; Kjell, M. H.; Zenkert, D.; Lindbergh, G.; Behm, M.; Willgert, M. Impact of electrochemical cycling on the tensile properties of carbon fibres for structural lithium-ion composite batteries. *Compos. Sci. Technol.* **2012**, *72*, 792–798.
- (21) Fredi, G.; Jeschke, S.; Boulaoued, A.; Wallenstein, J.; Rashidi, M.; Liu, F.; Harnden, R.; Zenkert, D.; Hagberg, J.; Lindbergh, G.; Johansson, P.; Stievano, L.; Asp, L. E. Graphitic microstructure and performance of carbon fibre Li-ion structural battery electrodes. *Multifunct. Mater.* **2018**, *1*, No. 015003.
- (22) Greenhalgh, E. S.; Ankersen, J.; Asp, L. E.; Bismarck, A.; Fontana, Q. P. V.; Houille, M.; Kalinka, G.; Kucernak, A.; Mistry, M.; Nguyen, S.; Qian, H.; Shaffer, M. S. P.; Shirshova, N.; Steinke, J. H. G.; Wienrich, M. Mechanical, Electrical and Microstructural Characterisation of Multifunctional Structural Power Composites. *J. Compos. Mater.* **2015**, *49*, 1823–1834.
- (23) Geier, S.; Petersen, J.; Iyer, V.; Wierach, P. In *Challenges of Integrating Supercapacitors into Structures for Space Qualification*, 16th European Conference on Spacecraft Structures, Materials and Environmental Testing (ECSSMET 2021); Braunschweig: Germany, 2021.
- (24) Qian, H.; Diao, H.; Shirshova, N.; Greenhalgh, E. S.; Steinke, J. H. G.; Shaffer, M. S. P.; Bismarck, A. Activation of structural carbon fibres for potential applications in multifunctional structural supercapacitors. *J. Colloid Interface Sci.* **2013**, *395*, 241–248.
- (25) Yu, Z.; Thomas, J. Energy Storing Electrical Cables: Integrating Energy Storage and Electrical Conduction. *Adv. Mater.* **2014**, *26*, 4279–4285.
- (26) Leijonmarck, S.; Carlson, T.; Lindbergh, G.; Asp, E. S.; Maples, H.; Bismarck, A. Solid polymer electrolyte coated carbon fibers for structural and novel micro batteries. *Compos. Sci. Technol.* **2013**, *89*, 149–157.
- (27) Carlstedt, D.; Asp, L. E. Performance analysis framework for structural battery composites in electric vehicles. *Composites, Part B* **2020**, *186*, No. 107822.
- (28) Snyder, J. F.; Carter, R. H.; Wetzel, E. D. In *Integrating Structure with Power in Battery Materials*, Proceedings of the 2004 Army Science Conference; DTIC: Orlando, Florida, USA, 2004.
- (29) Asp, L. E.; Johansson, M.; Lindbergh, G.; Xu, J.; Zenkert, D. Structural battery composites: a review. *Funct. Compos. Struct.* **2019**, *1*, No. 042001.
- (30) Kühnelt, H.; Beutl, A.; Mastropiero, F.; Laurin, F.; Willrodt, S.; Bismarck, A.; Guida, M.; Romano, F. Structural Batteries for Aeronautic Applications - State of the Art, Research Gaps and Technology Development Needs. *Aerospace* **2022**, *9*, No. 7.
- (31) Danzi, F.; Salgado, R. M.; Oliveira, J. E.; Arreiro, A.; Camanho, P. P.; Braga, M. H. Structural Batteries: A Review. *Molecules* **2021**, *26*, No. 2203.
- (32) Schneider, L. M.; Ihrner, N.; Zenkert, D.; Johansson, M. Bicontinuous Electrolytes via Thermally Initiated Polymerization for Structural Lithium Ion Batteries. *ACS Appl. Energy Mater.* **2019**, *2*, 4362–4369.
- (33) Dong, G.-H.; Mao, Y.; Yang, G.; Li, Y.; Song, S.; Xu, C.; Huang, P.; Hu, N.; Fu, S. High-Strength Poly(ethylene oxide) Composite Electrolyte Reinforced with Glass Fiber and Ceramic Electrolyte

Simultaneously for Structural Energy Storage. *ACS Appl. Energy Mater.* **2021**, *4* (4), 4038–4049.

(34) Li, D.; Chen, L.; Wang, T.; Fan, L. Z. 3D Fiber-Network-Reinforced Bicontinuous Composite Solid Electrolyte for Dendrite-free Lithium Metal Batteries. *ACS Appl. Mater. Interfaces* **2018**, *10*, 7069–7078.

(35) Kjell, M. H.; Zavalis, T. G.; Behm, M.; Lindbergh, G. Electrochemical Characterization of Lithium Intercalation Processes of PAN-Based Carbon Fibers in a Microelectrode System. *J. Electrochem. Soc.* **2013**, *160*, A1473–A1481.

(36) Hagberg, J.; Leijonmarck, S.; Lindbergh, G. High precision coulometry of commercial PAN-based carbon fibres as electrodes in structural batteries. *J. Electrochem. Soc.* **2016**, *163*, A1790–A1797.

(37) Donnet, J. B.; Wang, T. K.; Peng, J. C. M.; Rebouillat, S. *Carbon Fibers*, 3rd ed.; Marcel Dekker, 1998.

(38) Kjell, M. H.; Jacques, E.; Zenkert, D.; Behm, M.; Lindbergh, G. PAN-based carbon fibre electrodes for structural lithium-ion batteries. *J. Electrochem. Soc.* **2011**, *158*, A1455–60.

(39) Thomas, P.; Billaud, D. Sodium electrochemical insertion mechanisms in various carbon fibres. *Electrochim. Acta* **2001**, *46*, 3359–3366.

(40) Harnden, R.; Peuvot, K.; Zenkert, D.; Lindbergh, G. Multifunctional Performance of Sodiated Carbon Fibers. *J. Electrochem. Soc.* **2018**, *165* (13), B616–B622.

(41) Stevens, D. A.; Dahn, J. R. The Mechanisms of Lithium and Sodium Insertion in Carbon Materials. *J. Electrochem. Soc.* **2001**, *148* (8), A803–A811.

(42) Zhang, B.; Ghimbeu, C. M.; Laberty, C.; Vix-Guterl, C.; Tarascon, J. M. Correlation between Microstructure and Na Storage Behavior in Hard Carbon. *Adv. Energy Mater.* **2016**, *6* (1), No. 1501588.

(43) Zheng, T.; Liu, Y.; Fuller, E. W.; Tseng, S.; von Sacken, U.; Dahn, J. R. Lithium insertion in high capacity carbonaceous materials. *J. Electrochem. Soc.* **1995**, *142* (8), No. 2581.

(44) Danzi, F.; Camanho, P. P.; Braga, M. H. An All-Solid-State Coaxial Structural Battery Using Sodium-Based Electrolyte. *Molecules* **2021**, *26*, No. 5226.

(45) Valente, M.; Silva, S. M.; Braga, M. H. Cork: Enabler of sustainable and efficient coaxial structural batteries. *Heliyon* **2023**, *9* (4), No. e150631.

(46) Fenton, D. E.; Parker, J. M.; Wright, P. V. Complex of alkali metal ions with poly (ethylene oxide). *Polymer* **1973**, *14*, No. 589.

(47) Armand, M.; Chabagno, J.-M.; Duclot, M. J. In *Fast Ion Transport in Solids: electrodes and electrolytes*; Proceedings of Fast Ion Transport in Solids: Electrodes and Electrolytes Vashishta, P.; Mundy, J. N.; Shenoy, G. K., Eds.; Elsevier: Lake Geneva, WI, USA, 1979; Vol. 5.

(48) Zhou, W. D.; Li, Y. T.; Xin, S.; Goodenough, J. B. Rechargeable Sodium All-Solid-State Battery. *ACS Cent. Sci.* **2017**, *3*, 52–57.

(49) He, L.; Qiaomei, S.; Lu, L.; Adams, S. Understanding and Preventing Dendrite Growth in Lithium Metal Batteries. *ACS Appl. Mater. Interfaces* **2021**, *13* (29), 34320–34331.

(50) Kim, J. J.; Yoon, K.; Park, I.; Kang, K. Progress in the Development of Sodium-Ion Solid Electrolytes. *Small Methods* **2017**, *1*, No. 1700219.

(51) Hayashi, A.; Noi, K.; Sakuda, A.; Tatsumisago, M. Superionic glass-ceramic electrolytes for room-temperature rechargeable sodium batteries. *Nat. Commun.* **2012**, *3*, No. 856.

(52) Ma, Q. L.; Guin, M.; Naqash, S.; Tsai, C. L.; Tietz, F.; Guillon, O. Scandium-Substituted $\text{Na}_3\text{Zr}_2(\text{SiO}_4)_2(\text{PO}_4)$ Prepared by a Solution-Assisted Solid-State Reaction Method as Sodium-Ion Conductors. *Chem. Mater.* **2016**, *28*, 4821–4828.

(53) Young, W.-S.; Kuan, W.-F.; Epps, T. H. Block copolymer electrolytes for rechargeable lithium batteries. *J. Polym. Sci., Part B: Polym. Phys.* **2014**, *52* (1), 1–16.

(54) Borodin, O.; Smith, G. D. Mechanism of Ion Transport in Amorphous Poly(ethylene oxide)/LiTFSI from Molecular Dynamics Simulations. *Macromolecules* **2006**, *39* (4), 1620–1629.

(55) Goodenough, J. B.; Hong, H. Y. P.; Kafalas, J. A. Fast Na^+ ion transport in skeleton structures. *Mater. Res. Bull.* **1976**, *11*, 203–220.

(56) Hong, H. Y. P. Crystal structures and crystal chemistry in the system $\text{Na}_{1+x}\text{Zr}_2\text{Si}_x\text{P}_{3-x}\text{O}_{12}$. *Mater. Res. Bull.* **1976**, *11*, 173–182.

(57) Zhao, C.; Liu, L.; Qi, X.; Lu, Y.; Wu, F.; Zhao, J.; Yu, Y.; Hu, Y.-S.; Chen, L. Solid-State Sodium Batteries. *Adv. Energy Mater.* **2018**, *8* (17), No. 1703012.

(58) Ban, X. Y.; Zhang, W. Q.; Chen, N.; Sun, C. W. A High-Performance and Durable Poly(ethylene oxide) Based Composite Solid Electrolyte for All Solid-State Lithium Battery. *J. Phys. Chem. C* **2018**, *122*, 9852–9858.

(59) Yu, X.; Xue, L.; Goodenough, J. B.; Manthiram, A. A High-Performance All-Solid-State Sodium Battery with a Poly(ethylene oxide)- $\text{Na}_3\text{Zr}_2\text{Si}_2\text{PO}_{12}$ Composite Electrolyte. *ACS Mater. Lett.* **2019**, *1* (1), 132–138.

(60) ASTM-D638 Standards 2024. <https://www.zwickroell.com/industries/plastics/thermoplastics-and-thermosetting-molding-materials/tensile-properties-astm-d638/>. (accessed January, 2024).

(61) Evans, J.; Vincent, C. A.; Bruce, P. G. Electrochemical measurement of transference numbers in polymer electrolytes. *Polymer* **1987**, *28*, 2324–2328.

(62) Ge, Z.; Li, J.; Liu, J. High Sodium Ion Mobility of PEO- $\text{NaTFSI-Na}_3\text{Zr}_2\text{Si}_2\text{PO}_{12}$ Composite Solid Electrolyte for All-Solid-State Na-S Battery. *ChemistrySelect* **2022**, *7*, No. 202200620.

(63) Lee, B.; Paek, E.; Mitlin, D.; Lee, S. W. Sodium Metal Anodes: Emerging Solutions to Dendrite Growth. *Chem. Rev.* **2019**, *119* (8), 5416–5460.

(64) Qiang, Z.; Chen, Y. M.; Xia, Y. F.; Liang, W. F.; Zhu, Y.; Vogt, B. D. Ultra-long cycle life, low-cost room temperature sodium-sulfur batteries enabled by highly doped (N,S) nanoporous carbons. *NanoEnergy* **2017**, *32*, 59–66.

(65) Komaba, S.; Ishikawa, T.; Yabuuchi, N.; Murata, W.; Ito, A.; Ohsawa, Y. Fluorinated ethylene carbonate as electrolyte additive for rechargeable Na batteries. *ACS Appl. Mater. Interfaces* **2011**, *3*, 4165–4168.

(66) Feng, M.; Wang, S.; Yu, Y.; Feng, Q.; Yang, J.; Zhang, B. Carboxyl functionalized carbon fibers with preserved tensile strength and electrochemical performance used as anodes of structural lithium-ion batteries. *Appl. Surf. Sci.* **2017**, *392*, 27–35.

(67) Meng, C.; Muralidharan, N.; Teblum, E.; Moyer, K. E.; Nessim, G. D.; Pint, C. L. Multifunctional Structural Ultrabattery Composite. *Nano Lett.* **2018**, *18*, 7761–7768.

(68) Thakur, A.; Dong, X. Printing with 3D continuous carbon fiber multifunctional composites via UV-assisted coextrusion deposition. *Manuf. Lett.* **2020**, *24*, 1–5.

(69) Moyer, K.; Meng, C.; Marshall, B.; Assal, O.; Eaves, J.; Perez, D.; Karkkainen, R.; Roberson, L.; Pint, C. L. Carbon fiber reinforced structural lithium-ion battery composite: Multifunctional power integration for CubeSats. *Energy Storage Mater.* **2020**, *24*, 676–681.

(70) Asp, L. E.; Bouton, K.; Carlstedt, D.; Duan, S.; Harnden, R.; Johansson, W.; Johansen, M.; Johansson, M. K. G.; Lindbergh, G.; Liu, F.; Peuvot, K.; Schneider, L. M.; Xu, J.; Zenkert, D. A Structural Battery and its Multifunctional Performance. *Adv. Energy Sustainability Res.* **2021**, *2*, No. 2000093.

(71) Siraj, M. S.; Tasneem, S.; Carlstedt, D.; Duan, S.; Johansen, M.; Larsson, C.; Xu, J.; Liu, F.; Edgren, F.; Asp, L. E. Advancing Structural Battery Composites: Robust Manufacturing for Enhanced and Consistent Multifunctional Performance. *Adv. Energy Sustainability Res.* **2023**, *4*, No. 2300109.